Journal of Power Sources 195 (2010) 4160–4167

Contents lists available at ScienceDirect

Journal of Power Sources

journal homepage: www.elsevier.com/locate/jpowsour

Modeling of anode-supported SOFCs with samaria doped-ceria electrolytes operating at 500–600 °C

Daan Cui, Qiang Liu, Fanglin Chen*

Department of Mechanical Engineering, University of South Carolina, 300 Main Street, Columbia, SC 29208, United States

ARTICLE INFO

Article history:
Received 16 December 2009
Received in revised form 1 January 2010
Accepted 5 January 2010
Available online 13 January 2010

Keywords:
Solid oxide fuel cell (SOFC)
Ceria-based electrolyte
Isothermal model
Leakage current
Current efficiency

ABSTRACT

A two-dimensional isothermal mathematical model is developed for an anode-supported solid oxide fuel cell using samaria doped-ceria as electrolyte. This model takes into account species transfer and electrochemical reaction processes for cell operating between 500 °C and 600 °C. In this model, it is assumed that the electrochemical reactions take place not only at the electrolyte/electrode boundaries, but also throughout the electrodes. The model is validated with the experimental data. The geometry and operating parametric analyses are conducted to understand the coupled electrochemical reaction and species transfer phenomena. The results indicate that the rate of leakage current increases with the increase either in cell operating voltages, or in cell operating temperatures. It is also found that higher hydrogen concentration in the fuel stream results in larger leakage current. Further, the current efficiency decreases with the increase either in cell active areas, or in cell operating temperatures.

© 2010 Elsevier B.V. All rights reserved.

1. Introduction

Fuel cells, which directly convert chemical energy into electricity, have been well recognized as efficient, quiet, and environmentally benign energy conversion devices for power generation [1–3]. Among the different types of fuel cells, solid oxide fuel cells (SOFCs) have the advantages of fuel flexibility, fast reaction kinetics and high value waste heat suitable for downstream utilization to increase the overall system efficiency. In addition, SOFCs can utilize cost effective materials as catalysts, electrolytes, interconnects, and other structural components. Most importantly, the use of solid electrolyte in SOFCs eliminates the involvement of liquids and the variation of the electrolyte compositions during operation. Because all components are solid, SOFCs can be fabricated in very thin layers [4,5], and cell components can be configured into unique shapes unachievable in the other types of fuel cells. However, the cost of current SOFC systems is still prohibitive for wide-spread commercial deployment. Reducing the operating temperature to 500–600 °C can dramatically reduce the cost of SOFC systems since relatively inexpensive metallic components can be used for bipolar plates, interconnects, heat exchangers, manifolding and other structural components in the SOFC system. Furthermore, it is also less difficult in sealing at lower operating temperatures. Lowering the operation temperature can also offer quick start-up ability, which in turn can enable SOFC for applications such as portable power sources and auxiliary power units for automobiles. A lower operating temperature would also ensure a greater overall system stability and durability, leading to longer expected lifetime for SOFC systems [6–8].

The current generation of SOFCs is based on yttria stabilized zirconia (YSZ) electrolyte due to its desirable strength and stability in both oxidizing and reducing atmospheres and its oxygen ion dominant conductivity [9]. Doped-ceria, such as samaria doped-ceria (SDC), can provide a higher conductivity than that of YSZ while operating at temperatures around 550 °C [10]. Doped-ceria-based electrolytes therefore allow fuel cell operation down to 600 °C [11–13]. However, leakage current occurs when doped-ceria materials are used as electrolytes because electronic conductivity of ceria-based materials is high at reducing environments or at high operating temperatures. Consequently, for SOFCs using ceria-based electrolytes, cell geometry and operating conditions have significant effects on the cell efficiency. Since the leakage current is difficult to measure under cell operating conditions, the current flow phenomena in SOFCs with doped-ceria electrolytes might be better analyzed through mathematical modeling.

However, previous modeling efforts mainly focus on SOFCs with YSZ electrolytes [14–17]. Only very limited reports have been published on SOFCs with ceria-based electrolytes [12,18–20]. Leah et al. [12] analyzed a metal-supported SOFC using gadolinia-doped-ceria (CGO) as the electrolyte through a zero dimension model. This cell model was then incorporated into a model of a 2.5 kW stack. This model did not consider the effect of cell geometry on cell efficiency. Up to now, a detailed finite element method (FEM) model has not been developed to study SOFCs with ceria-based electrolytes.

* Corresponding author. Tel.: +1 803 777 4875; fax: +1 803 777 0106.
E-mail address: chenfa@cec.sc.edu (F. Chen).

0378-7753/$ – see front matter © 2010 Elsevier B.V. All rights reserved.
doi:10.1016/j.jpowsour.2010.01.013

Nomenclature

c	concentration [mol m^{-3}]
D_{ij}	diffusion coefficient [m^2 s^{-1}]
$E_{cat,a}$	anode activation energy [J mol^{-1}]
$E_{cat,c}$	cathode activation energy [J mol^{-1}]
F	Faraday's constant [96,485 C mol^{-1}]
i	local current density [A m^{-2}]
k	Boltzmann constant [1.38e–23 J K^{-1}]
n_e	electron transferred per reacting [–]
P	pressure [Pa]
q	elementary charge [1.6e–19 C]
Q	current source term [A m^{-3}]
R_g	gas constant [8.314 J mol^{-1} K^{-1}]
R_i	the reaction rate [mol m^{-3} s^{-1}]
T	temperature [K]

Greek letters

β	transfer coefficient [–]
ε	porosity [–]
τ	tortuosity factor [–]
σ	conductivity [S m^{-1}]
ϕ	potential [V]

Subscripts and superscripts

a	anode
c	cathode
ele	electrolyte
rev	reversible
0	standard

The objectives of this work are to develop a two-dimensional (2D) FEM model to study cell geometry and operating condition effects on current efficiency of SOFCs with ceria-based electrolytes, and to understand the phenomena that occur in SOFCs operating at reduced temperatures. In the present work, a working SOFC with ceria-based electrolyte, Ni–ceria cermet anode and $La_{0.6}Sr_{0.4}Co_{0.2}Fe_{0.8}O_3$ (LSCF) cathode will be used to validate the 2D model. The model will cover the electrochemical reaction and electrical and species transport, and the corresponding equations in this model can be solved through FEM.

2. Experimental

The $La_{0.6}Sr_{0.4}Co_{0.2}Fe_{0.8}O_3$ (LSCF) and $Sm_{0.2}Ce_{0.8}O_{1.95}$ (SDC) powders were synthesized by the glycine–nitrate process (GNP). Anode-supported thin electrolyte bilayer assemblies were fabricated by one-step dry-pressing method. Green bodies consisting of NiO–SDC substrates and SDC electrolytes were formed by co-pressing the anode powder and SDC powder into a pellet using a uniaxial die-press (13 mm in diameter). The bilayer including the anode and electrolyte was sintered at 1350 °C in air for 5 h. A LSCF cathode (area 0.33 cm^2) was slurry coated on the SDC electrolyte and fired at 1000 °C for 3 h.

Fig. 1 shows the schematic diagram of the cell test setup. Two gas chambers were set up by placing the cell at the end of an alumina tube. Ag wires were used as the cathode and anode lead wire and were attached to the electrodes with Ag paste. The single cell was mounted on an alumina tube by using a silver paste and sealed using a glass sealant. After NiO was reduced to Ni in situ by flowing H_2 at 600 °C, the cell performance was measured at 500–600 °C by changing an external load. The *I–V* characteristics of the anode-supported cell were evaluated using humidified hydrogen (3 vol% H_2O) as fuel (with a fuel flow rate of 40 ml min^{-1}) and ambient air as the oxidant.

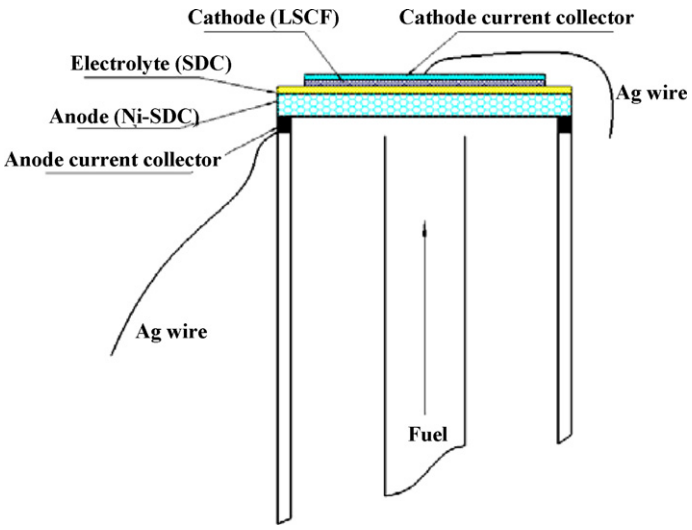

Fig. 1. Schematic diagram of the cell test setup.

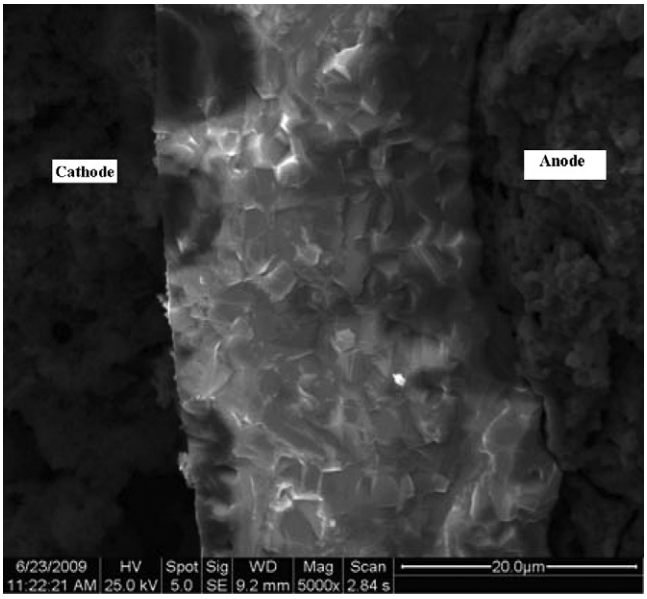

Fig. 2. Cross-sectional SEM graph of the single cell.

After testing, the cell was cooled down to room temperature while maintaining hydrogen flowing to the anode. The fracture surface of the cell was characterized by scanning electron microscopy (SEM, FEI Quanta 200), with a representative image shown in Fig. 2. The thickness of each layer was determined from the SEM micrographs.

3. Model developments

3.1. Model assumptions and geometry

The following assumptions are used to develop the model:

(1) The model is based on the cell steady state operation using humidified H_2 as the fuel.
(2) The reactant gas mixture is approximated as an ideal gas.
(3) The model is assumed to be isothermal.

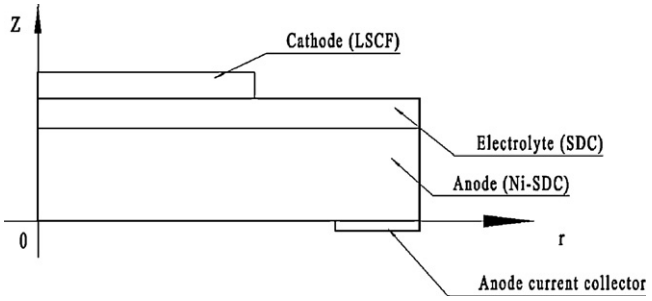

Fig. 3. Schematic diagram of modeling geometry.

Table 1
Input parameters to model [12,13,15].

Descriptions	Symbol	Value
Anode thickness (mm)		0.35
Cathode thickness (μm)		20
Electrolyte thickness (μm)		20
Anode radius (mm)		5.9
Electrolyte radius (mm)		5.9
Cathode radius (mm)		3.26
Anode conductivity ($S\,m^{-1}$)		80,000
Cathode electronic conductivity ($S\,m^{-1}$)		8400
Cathode ionic conductivity ($S\,m^{-1}$)		1.39×10^{9} $\exp(-1.32/(8.6173\times10^{-5}\cdot T))$
Transfer coefficient	β	0.5
Activation energy of anode ($J\,mol^{-1}$)	$E_{act,a}$	129,400
Activation energy of cathode ($J\,mol^{-1}$)	$E_{act,a}$	130,900
Reaction active area ($m^2\,m^{-3}$)	S_{TPB}	3×10^{5}
Porosity	ε	30%
Tortuosity factor	τ	10
Electron transferred per reacting	n_e	1

(4) The reaction active sites are uniformly distributed in electrodes.
(5) The pressure driven flow in porous electrodes is neglected.

The model geometry is based on a button cell. Due to the cell symmetry conditions, a two-dimensional axial symmetry coordinate is adopted as illustrated in Fig. 3. The material properties are listed in Table 1.

3.2. Charge balance

The charge balance governing domains include the anode, the cathode and the electrolyte. At the electrodes and the electrolyte, both electrons and oxygen ions are served as conducting species. The charge balance at the electrodes can be formulated by the Ohm's law:

$$-\nabla(\sigma\cdot\nabla\phi) = Q_j \tag{1}$$

The current source term Q_j can be calculated by the equation below.

$$Q_j = i_j S_{TPB} \tag{2}$$

where S_{TPB} in the above equation is the electrochemical reaction active area per unit volume and is kept as a constant in the calculation, while i_j is the local charge transfer current density which can be generally obtained through the Butler–Volmer kinetic equations:

$$i_a = i_{a,0}^{H_2}\cdot\frac{(p_{H_2})^{0.25}}{(p_{H_2O})^{0.5}}\exp\left(\frac{-E_{act,a}}{R\cdot T}\right)\cdot\left\{\exp\left(\beta\frac{n_e\cdot F\cdot(\phi_{rev}-|\phi_a-\phi_{ele}|)}{R_g\cdot T}\right)-\exp\left[-(1-\beta)\frac{n_e\cdot F\cdot(\phi_{rev}-|\phi_a-\phi_{ele}|)}{R_g\cdot T}\right]\right\} \tag{3}$$

$$i_c = i_{c,0}^{O_2}\cdot\exp\left(\frac{-E_{act,c}}{R\cdot T}\right)\cdot\left\{\exp\left(\beta\frac{n_e\cdot F\cdot(\phi_{rev}-|\phi_c-\phi_{ele}|)}{R_g\cdot T}\right)-\exp\left[-(1-\beta)\frac{n_e\cdot F\cdot(\phi_{rev}-|\phi_c-\phi_{ele}|)}{R_g\cdot T}\right]\right\} \tag{4}$$

Since several parameters could not be obtained directly from experiments or open literatures, tuning processes have to be involved in this study. In Eqs. (3) and (4), $i_{a,0}^{H_2}$ and $i_{c,0}^{O_2}$ are adjustable parameters for fitting the experimental data. $i_{a,0}^{H_2}$ is $1\times10^{11}\,A\,m^{-2}$ for the anode and $i_{c,0}^{O_2}$ is $7\times10^{10}\,A\,m^{-2}$ for the cathode in this study, respectively. ϕ_{rev} can be obtained from the Nernst equation. Electron and ion charge conservation at the electrolyte is expressed by Eq. (5).

$$-\nabla(\sigma\cdot\nabla\phi) = 0 \tag{5}$$

It is well known that a doped-ceria electrolyte behaves as a mixed conductor under typical cell operating conditions. For ceria-based electrolytes, the formation of Ce^{3+} cation results in electronic conductivity under reducing conditions. The oxygen ionic conductivity of SDC (σ_i) is normally affected by temperature, but the electronic conductivity (σ_e) is influenced by both the temperature and the local oxygen partial pressure $p_{O_2,el}$ [10]. The oxygen ionic conductivity (σ_i) and electronic conductivity (σ_e) of doped-ceria electrolytes can be expressed as:

$$\sigma_i = \sigma_{0,i}\exp\frac{(-E_{a,i}/(kT))}{T} \tag{6}$$

$$\sigma_e = \sigma_{0,e}(p_{O_2,el})^{-1/4}\exp\frac{(-E_{a,e}/(kT))}{T} \tag{7}$$

In this study, the electronic and ionic conductivities and activation energies are obtained by fitting the *I–V* curves of cell at different operating temperatures. The following

Table 2
Boundary conditions.

Boundary	Ionic charge	Electronic charge	Mass transfer
Anode/electrolyte interface	Continuity	Continuity	Insulation
Anode/channel interface	Insulation	Insulation	Fuel concentration
Anode/anode current collector interface	Insulation	$V_{cell,an}$	Insulation
Cathode/channel interface	Insulation	$V_{cell,ca}$	Oxygen concentration
Cathode/electrolyte interface	Continuity	Continuity	Insulation
Symmetry axis	Symmetry	Symmetry	Symmetry
Others	Insulation	Insulation	Insulation

values are obtained: $\sigma_{0,i} = 1.65 \times 10^6\ \mathrm{S\,K\,m^{-1}}$, $E_{a,i} = 0.5618\ \mathrm{eV}$; $\sigma_{0,e} = 3.184 \times 10^{12}\ \mathrm{S\,K\,m^{-1}}$, and $E_{a,e} = 2.8548\ \mathrm{eV}$. The electronic conductivity of SDC under cell operating conditions depends on the voltage of the cell and the thickness of the electrolyte. An equation of electronic conductivity of SDC is developed from the electron concentrations (per unit volume) at different positions [17,18].

$$\sigma_{(x)} = \sigma_{(\mathrm{cat})} \cdot \exp(\beta \cdot V_{\mathrm{th}}) \cdot \left[1 - \frac{1 - \exp(-\beta \cdot V_{\mathrm{th}})}{1 - \exp\left(-\beta \cdot \frac{\partial\varphi}{\partial x}\right) \cdot L} \cdot \left(1 - \exp\left(-\beta \cdot \frac{\partial\varphi}{\partial x} \cdot x\right)\right)\right] \quad (8)$$

$\beta = q/(k \cdot T)$; L is the thickness of the electrolyte; x is the distance to the anode/electrolyte interface; $\sigma_{(\mathrm{cat})}$ is electronic conductivity of SDC at the cathode side which is calculated from Eq. (7); V_{th} is the Nernst potential; $\partial\varphi/\partial x$ is the electric field in the electrolyte with the unit of $\mathrm{V\,m^{-1}}$.

3.3. Mass balance

The steady state diffusion equation, Eq. (9) is solved to obtain the species distribution in all domains.

$$\nabla\left(-D_{ij} \cdot \nabla c_i\right) = R_i \quad (9)$$

$$R_{O_2} = -\frac{i_c}{(4F)}; \quad R_{H_2} = -\frac{i_a}{(2F)}; \quad R_{H_2O} = \frac{i_a}{(2F)} \quad (10)$$

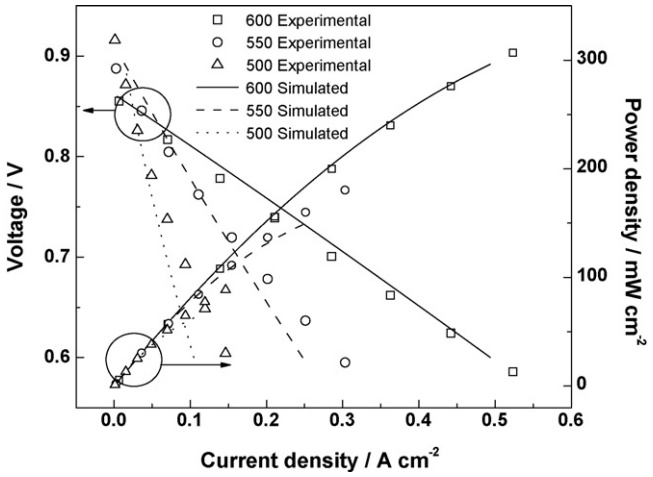

Fig. 4. Comparison of model-predicted and experimental *V–I* and power curves for a SOFC cell using SDC electrolyte operated at different temperatures (500 °C, 550 °C and 600 °C) with a fuel mixture of 97 vol% H_2/3 vol% H_2O.

Mass diffusion coefficients are required when species transport equations in multi-component flows are solved. For the electrodes in this model, both the Knudsen and the ordinary molecular diffusion processes have to be considered together and the overall effective diffusion coefficient is given as follows:

$$D_i = \frac{\varepsilon\left((1/D_{i,\mathrm{m}}) + (1/D_{\mathrm{K}})\right)^{-1}}{\tau} \quad (11)$$

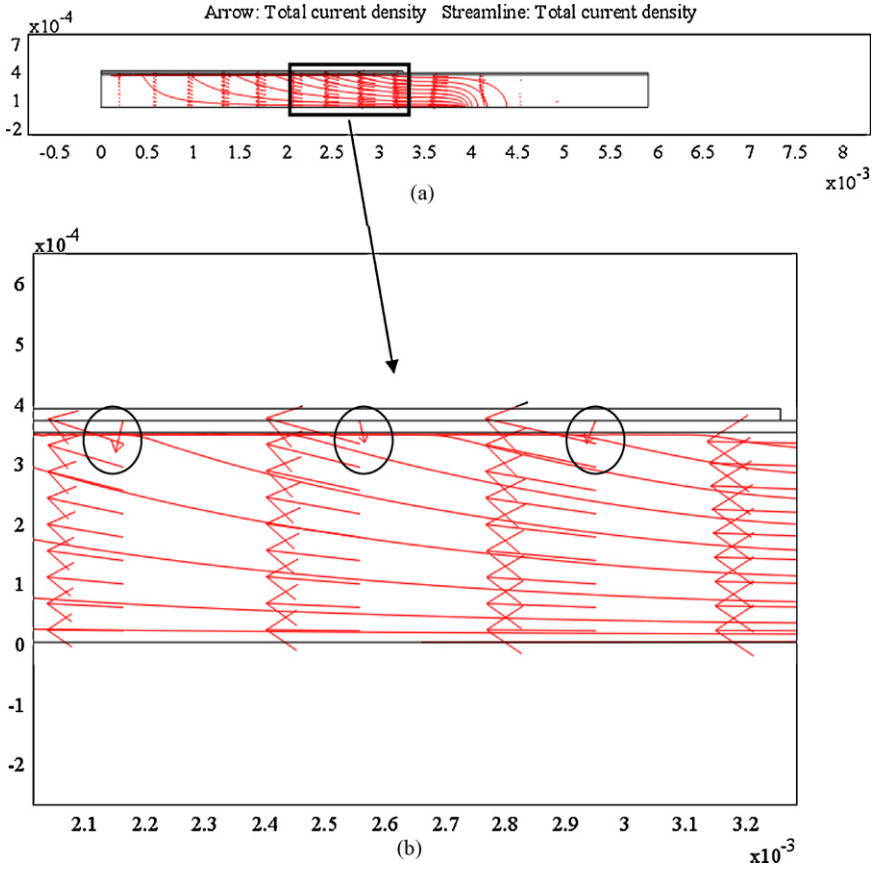

Fig. 5. The streamline and arrow plots of the anodic current density at 600 °C with a cell voltage of 0.8 V. The local part of figure (a) is scaled up to (b).

where ε denotes the porosity of a porous medium, τ stands for the tortuosity factor, $D_{i,m}$ and D_K designate the ordinary and Knudsen diffusion coefficients, respectively.

3.4. Boundary conditions

In order to solve the partial differential equations for charge and mass balances, the boundary conditions are shown in Table 2. The difference between $V_{cell,ca}$ and $V_{cell,an}$ is the cell voltage used in the calculation. $V_{cell,an}$ is defined as 0 V. In the boundary conditions, both "Insulation" and "Symmetry" mean that the partial derivative of a variable at the boundary is zero.

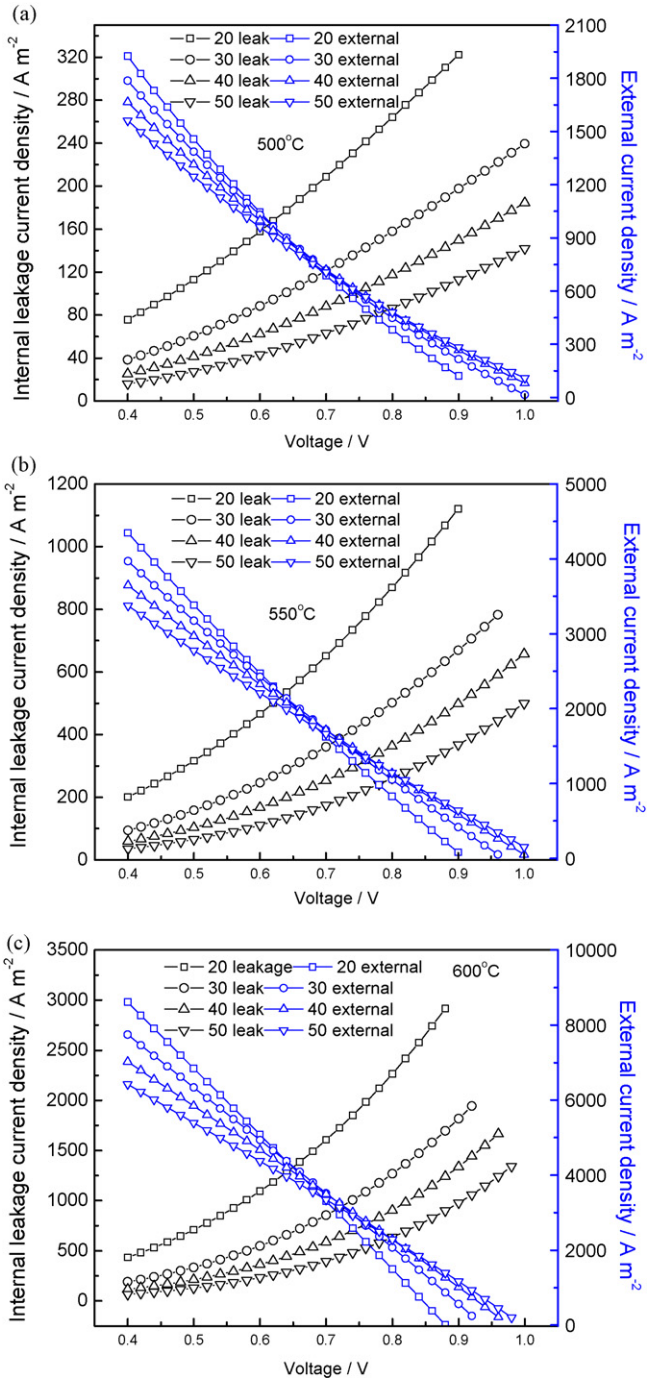

Fig. 6. Model-predicted electronic leakage current density and external circuit current density as a function of cell voltages and SDC electrolyte thicknesses (20 μm, 30 μm, 40 μm and 50 μm) at different cell operating temperatures with a fuel mixture of 97 vol% H_2/3 vol% H_2O.

3.5. Numerical solution

The governing equations are solved with commercial software, COMSOL Multiphsics. In the present study, a free mesh consisting of triangular elements for the 2D geometry is created in COMSOL Multiphysics. With the cell voltage changed, the cell performances were obtained from the model. The outputs from the model are the distributions of current density and species concentrations.

4. Results and discussion

4.1. Model validation

Fig. 4 shows the comparison of model-predicted and experimental *I–V* and power curves for a SOFC cell using SDC electrolyte operated at different temperatures. The simulation results show that the calculated polarization curves agree very well with the experimental data, especially at lower current densities or higher operating temperatures. The experimental data are higher than those of the calculated ones at higher current densities or lower operating temperatures. This discrepancy might be due to temperature differences caused by Ohmic heating at higher current densities in the experiments. The overall consistency between the experimental data and the simulated results indicates that the present model is accurate enough for studying the cell behavior.

4.2. Current density distribution in the cell

The streamline and arrow plots of the anodic current densities at 600 °C with a cell voltage of 0.8 V are shown in Fig. 5. The local part of Fig. 5(a) is scaled up to Fig. 5(b). The streamlines and arrows express current flow directions and paths, and the arrow lengths are proportional to current density. Due to the anode current collector located at the edge of the cell, the current flow into anode from the cell edge to the center. The current coming into anode is mainly from a point which locates inside the anode current collector since the current path is shortest when current flow in the anode from inside current collector. From Fig. 5, it is also seen that the leakage current flow into the anode from the electrolyte in the black circle.

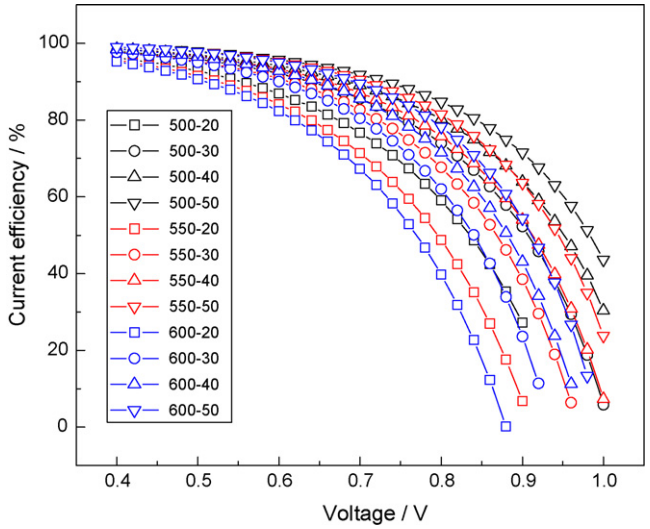

Fig. 7. Model-predicted current efficiency as a function of cell voltages, operating temperatures and SDC electrolyte thicknesses (20 μm, 30 μm, 40 μm and 50 μm) with a fuel mixture of 97 vol% H_2/3 vol% H_2O.

4.3. Electrolyte thickness dependence

The model-predicted electronic leakage current density and external circuit current density are determined as a function of cell voltages and SDC electrolyte thicknesses (20 μm, 30 μm, 40 μm and 50 μm) at different cell operating temperatures with a fuel mixture of 97 vol% H_2/3 vol% H_2O, as illustrated in Fig. 6. The leakage current is different under different electrolyte thicknesses. For thicker electrolytes, the leakage current is insignificant. When the thickness of the electrolyte decreases, the leakage current density increases. Further, the leakage current decreases when lowering the cell output voltage. For the different electrolyte thicknesses, the change of the external current is different at a given cell voltage. As shown in Fig. 6(a), when the cell voltage is more than 0.65 V, the external current of the cell is higher for the thicker electrolyte. Whereas, when the cell voltage is less than 0.65 V, the external current of the cell is higher for the thinner electrolyte. This is due to the fact that the increasing rate of the leakage current at higher cell voltage is faster than that at lower cell voltage. Consequently, more leakage current results in less external current for the cells with thinner electrolytes when the cell voltage is high. For a given thickness of the electrolyte, the cell external current decreases with an increase in the cell voltage. For a cell with an electrolyte thickness of 20 μm, the external current density increases from 687 A m^{-2} to 1624 A m^{-2} at a cell voltage of 0.7 V when the cell temperature increases from 500 °C to 550 °C. The leakage current increases from 209 A m^{-2} to 651 A m^{-2} for the cell operating at the same conditions. Comparing Fig. 6(a)–(c), the increasing rate of leakage current is larger than that of the external current with the increase in cell operating temperature.

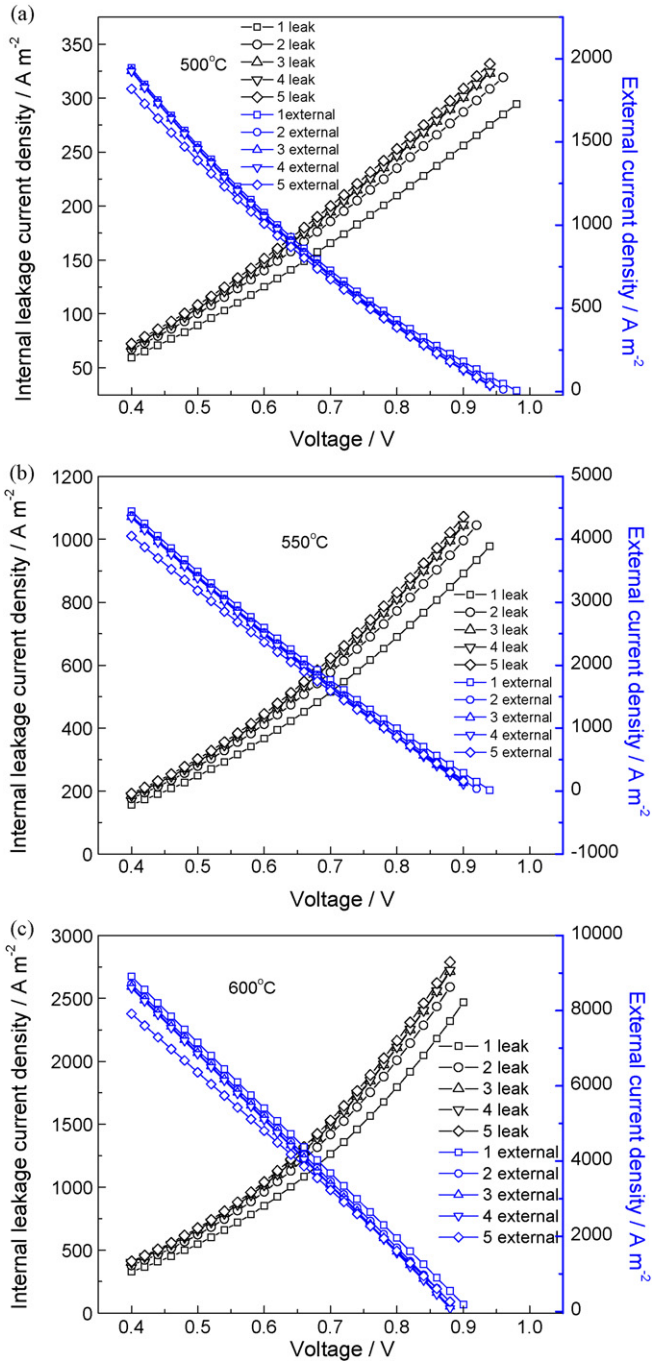

Fig. 8. Model-predicted electronic leakage current density and external circuit current density as a function of cell voltages and cathode radii (1 mm, 2 mm, 3 mm, 4 mm and 5 mm) at different operating temperatures with a fuel mixture of 97 vol% H_2/3 vol% H_2O.

The model-predicted current efficiencies are given in Fig. 7 as a function of cell voltages, operating temperatures as well as SDC electrolyte thicknesses (20 μm, 30 μm, 40 μm and 50 μm) with a fuel mixture of 97 vol% H_2/3 vol% H_2O. The current efficiency is calculated through Eq. (12):

$$\text{Current efficiency} = \frac{\text{External current}}{(\text{External current} + \text{Leakage current})} \quad (12)$$

As shown in Fig. 7, with the increase in cell voltages, the current efficiency decreases. At higher cell voltages, especially above 0.6 V, the decreasing rate of current efficiency is faster than that at lower voltages. With the increase in the electrolyte thickness, the current efficiency increases. For the same electrolyte thickness, current efficiency is lower at higher operating temperatures. The current efficiency of a cell at 500 °C with an electrolyte thickness of 40 μm is close to that of a cell at 550 °C with an electrolyte thickness of 50 μm. Furthermore, the current efficiency of a cell at 500 °C with an electrolyte thickness of 40 μm is close to that of a cell at 600 °C with an electrolyte thickness of 50 μm.

4.4. Cell active area dependence

The model-predicted electronic leakage current density and external circuit current density are shown in Fig. 8 as a function

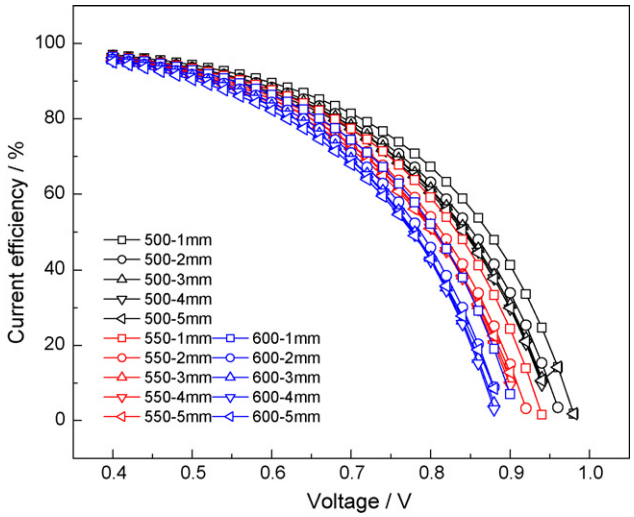

Fig. 9. Model-predicted current efficiency as a function of cell voltages and cathode radii (1 mm, 2 mm, 3 mm, 4 mm and 5 mm) with a fuel mixture of 97 vol% H_2/3 vol% H_2O.

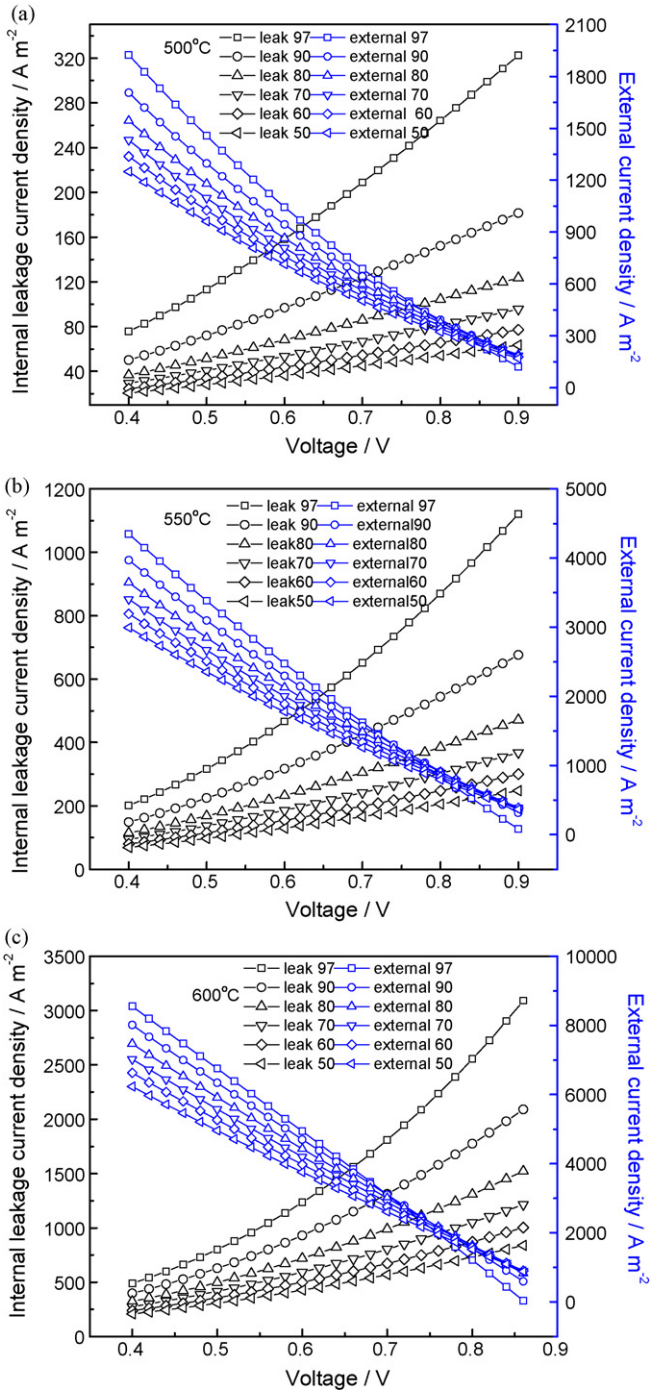

Fig. 10. Model-predicted electronic leakage current density and external circuit current density as a function of cell voltages and H_2 mole fractions (97%, 90%, 80%, 70%, 60% and 50%) at different cell operating temperatures.

of cell voltages and cathode radii (1 mm, 2 mm, 3 mm, 4 mm and 5 mm) at different operating temperatures with a fuel mixture of 97 vol% H_2/3 vol% H_2O. With the decrease in cell voltages, the leakage current decreases. The cell active area is directly related to cathode radii. From the current–voltage curves given in Fig. 8, it can be seen that the leakage and external current are different under different cell active areas: the smaller the cell active area, the less the cell leakage current. For a given active area, the external current decreases with the increase in the cell voltage. Furthermore, the external current decreases with an increase in the cell active area. As shown in Fig. 8, the open circuit voltage (OCV) decreases with the

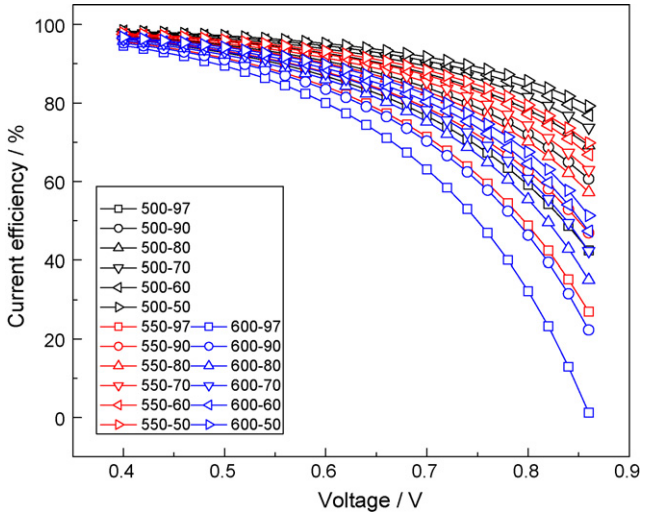

Fig. 11. Model-predicted current efficiency as a function of cell voltages and H_2 mole fractions (97%, 90%, 80%, 70%, 60% and 50%) at different cell operating temperatures.

increase in the cell active area. At a cathode radius of 1 mm, the cell OCV is obviously higher than those of the others with larger cathode radii. Consequently, for SOFCs using doped-ceria electrolytes, the change of cell OCVs should be carefully investigated especially when a larger foot-print cell is used.

For the cell with a cathode radius of 1 mm, the external current increases from 727 A m^{-2} to 1763 A m^{-2} at a cell voltage of 0.7 V when the cell temperature increases from 500 °C to 550 °C. The leakage current increases from 165 A m^{-2} to 515 A m^{-2} for the cell operating under the same conditions. It is similar to the results shown in Fig. 7 where the increasing rate of leakage current is larger than that of the external current with the increase in cell operating temperatures.

The model-predicted current efficiency is shown in Fig. 9 as a function of cell voltages, operating temperatures and cathode radii (1 mm, 2 mm, 3 mm, 4 mm and 5 mm) with a fuel mixture of 97 vol% H_2/3 vol% H_2O. The current efficiency is calculated through Eq. (12). It can be seen that the current efficiency decreases with the increase either in cell voltage or in the cell active area. For a given cell active area, the current efficiency is lower at a higher operating temperature.

4.5. Fuel composition dependence

The model-predicted electronic leakage current density and external circuit current density are investigated as a function of cell voltages and H_2 mole fractions (97%, 90%, 80%, 70%, 60% and 50%) at different cell operating temperatures, as shown in Fig. 10. The fuel is composed of a mixture of hydrogen and water vapor, i.e., when H_2 mole fraction is 70%, the water vapor mole fraction is 30%. The leakage current is different at different fuel compositions. For higher hydrogen concentrations, the leakage current is larger. When the hydrogen concentration decreases, the leakage current density decreases correspondingly. Furthermore, the leakage current decreases with the decrease in cell voltages. For different hydrogen concentrations, the change of external current is different at a given cell voltage. With the increase in hydrogen concentrations, the external current increases at lower cell voltage. As illustrated in Fig. 10, when the cell voltage is above 0.8 V, external current of the cell is very close for different hydrogen concentrations.

The model-predicted cell current efficiency is given as a function of cell voltages and H_2 mole fractions (97%, 90%, 80%, 70%,

60% and 50%) at different cell operating temperatures, as shown in Fig. 11. The cell current efficiency is calculated through Eq. (12). It can be seen that the cell current efficiency decreases with an increase either in cell voltages or in hydrogen concentrations. For a given hydrogen concentration, the cell current efficiency is lower at higher temperatures.

5. Conclusions

A 2D numerical model considering species transfer and electrochemical phenomena has been developed and proved to be valuable and efficient for cell performance analyses of SOFCs using ceria-based electrolytes. The variations of species concentrations and 2D distribution of current density have been obtained. The validation results show that the model agrees well with the experimental data. The 2D distribution of current streamline illustrates that the current flowing into the anode comes mainly from a point located inside the anode current collector. With the increase in cell voltages, the leakage current increases and the current efficiency decreases. Thicker electrolytes result in smaller leakage current and larger current efficiency. At higher cell voltages, the increasing rate of leakage current is faster than that at lower cell voltage. The increasing rate of leakage current is larger than that of the external current with the increase of cell operating temperatures. The cell OCV as well as cell current efficiency decrease with the increase of cell active areas. Higher hydrogen concentration in fuel streams results in larger leakage current and consequently lower current efficiency. The model can help understand the phenomena occurring in SOFCs using ceria-based electrolytes and offer guidance in the optimization of cell geometries and cell operating conditions.

Acknowledgments

This material is based upon work supported as part of the Science Based Nano-Structure Design and Synthesis of Heterogeneous Functional Materials for Energy Systems, an Energy Frontier Research Center funded by the U.S. Department of Energy, Office of Science, Office of Basic Energy Sciences under Award Number DE-SC0001061.

References

[1] D.J.L. Brett, A. Atkinson, N.P. Brandon, S.J. Skinner, Chem. Soc. Rev. 37 (2008) 1568–1578.
[2] R.M. Ormerod, Chem. Soc. Rev. 32 (2003) 17–28.
[3] M.D. Gross, J.M. Vohs, R.J. Gorte, J. Mater. Chem. 17 (2007) 3071–3077.
[4] D. Yang, X. Zhang, S. Nikumb, C. Deces–Petit, R. Hui, R. Maric, D. Ghosh, J. Power Sources 164 (2007) 182–188.
[5] A. Evans, A. Bieberle-Hutter, H. Galinski, J.L.M. Rupp, T. Ryll, B. Scherrer, R. Tolke, L.J. Gauckler, Chem. Month. 140 (2009) 975–983.
[6] Q. Liu, X. Dong, C. Yang, S. Ma, F. Chen, J. Power Sources 195 (2010) 1543–1550.
[7] F. Zhao, R.R. Peng, C.R. Xia, Mater. Res. Bull. 43 (2008) 370–376.
[8] M. Yang, A. Yan, M. Zhang, Z. Hou, Y. Dong, M. Cheng, J. Power Sources 175 (2008) 345–352.
[9] W. Weppner, J. Solid State Chem. 20 (1977) 305–314.
[10] K. Wang, R. Ran, W. Zhou, H. Gu, Z. Shao, J. Ahn, J. Power Sources 179 (2008) 60–68.
[11] B.C.H. Steele, Solid State Ionics 129 (2000) 95–110.
[12] R.T. Leah, N.P. Brandon, P. Aguiar, J. Power Sources 145 (2005) 336–352.
[13] D. Ding, L. Li, K. Feng, Z.B. Liu, C.R. Xia, J. Power Sources 187 (2009) 400–402.
[14] D. Cui, L. Liu, Y. Dong, M. Cheng, J. Power Sources 174 (2007) 246–254.
[15] D. Cui, M. Cheng, AICHE J. 55 (2009) 771–782.
[16] D. Cui, M. Cheng, J. Power Sources 192 (2009) 400–407.
[17] D. Cui, M. Cheng, J. Power Sources 195 (2010) 1435–1440.
[18] M. Liu, H. Hu, J. Electrochem. Soc. 143 (1996) L109–L112.
[19] I. Riess, J. Phys. Chem. Solids 47 (1986) 129–138.
[20] I. Riess, M. Giidickemeier, L.J. Gauckler, Solid State Ionics 90 (1996) 91–104.